

Flight Measurements of the Aero-Optical Environment Around a Flat-Windowed Turret

Chris Porter,* Stanislav Gordeyev,† Mike Zenk,‡ and Eric Jumper§
University of Notre Dame, Notre Dame, Indiana 46545

DOI: 10.2514/1.J052067

This paper discusses the aero-optical environment for a flat-window hemisphere-on-cylinder turret over a wide range of viewing angles during flight tests in the Airborne Aero-Optics Laboratory. Aero-optical aberrations around the turret were measured using a high-speed Shack–Hartmann wave-front sensor providing an extensive aero-optical mapping. The primary data were acquired at Mach 0.5 at an altitude of 15,000 ft, with a subset of the data collected at Mach 0.4 for verification of scaling relationships. Data were acquired holding the relative position between two aircrafts constant. Additional data sets were acquired allowing two aircrafts to change their relative positions so that slewing data could be acquired; this provided statistical data over a large range of viewing angles between looking-forward to looking-back angles. Results were analyzed, and the aero-optical contribution from different flow features over the turret was identified and discussed. Cross-correlation functions and convective speed were also computed for some viewing angles and compared with other experiments. The flight-test data were also compared to wind-tunnel measurements using the identical turret.

Nomenclature

| | | |
|--------------------|---|--|
| A_D | = | aperture diameter |
| A_z | = | azimuthal angle |
| D | = | turret diameter |
| El | = | elevation angle |
| K_{GD} | = | Gladstone–Dale constant |
| M | = | incoming Mach number |
| n | = | index of refraction |
| OPD | = | optical path difference |
| OPD _{RMS} | = | spatial rms of the optical path difference |
| OPL | = | optical path length |
| t | = | time |
| s | = | integration variable |
| \mathbf{x} | = | position vector |
| x, y, z | = | turret coordinates |
| x_A, y_A | = | aperture coordinates |
| α | = | viewing angle |
| β | = | modified elevation angle |
| ρ | = | density |
| ρ_o | = | free-stream density |
| ρ_{SL} | = | sea-level density |
| λ | = | wavelength |

I. Introduction

IN THE late 1970s and early 1980s, optical turrets were extensively studied as the use of lasers on aircraft started to become

Presented as Paper 2011-3280 at the 42th Plasmadynamics and Lasers Conference, Honolulu, HI, 27–30 June 2011; received 3 May 2012; revision received 26 December 2012; accepted for publication 4 January 2013; published online 23 April 2013. Copyright © 2013 by Porter, Gordeyev, Zenk and Jumper. Published by the American Institute of Aeronautics and Astronautics, Inc., with permission. Copies of this paper may be made for personal or internal use, on condition that the copier pay the \$10.00 per-copy fee to the Copyright Clearance Center, Inc., 222 Rosewood Drive, Danvers, MA 01923; include the code 1533-385X/13 and \$10.00 in correspondence with the CCC.

*National Research Council Associate, Department of Aerospace Engineering, U.S. Air Force Academy, Colorado Springs, CO 80840. Member AIAA.

†Research Associate Professor, Department of Mechanical and Aerospace Engineering, Hessert Laboratory for Aerospace Research. Associate Fellow AIAA.

‡Project Manager, Department of Mechanical and Aerospace Engineering, Hessert Laboratory for Aerospace Research. Member AIAA.

§Professor, Department of Mechanical and Aerospace Engineering, Hessert Laboratory for Aerospace Research. Fellow AIAA.

feasible. During that period, the Airborne Laser Laboratory (ALL) successfully demonstrated the usefulness of airborne lasers [1]. The ALL carbon-dioxide laser's long wavelength (10.6 μm) limited the range and irradiance that the system could deliver on target. With new, more-powerful lasers came the ability to deliver more laser energy onto a target and an increased range. However, the shorter wavelength (1–1.5 μm) of these new lasers increased the detrimental effects that inhomogeneous refractive mediums [2–4] have on the ability of optical systems to focus a laser beam in the far field.

With the new potential of these lasers, achieving a maximum field of regard is a necessity. Hemisphere-on-cylinder turrets offer a simple, mechanically efficient means to project or receive laser radiation to or from a target over a full field of regard; however, the flow around a turret consists of a separated wake region aft of the turret, where pressure and temperature fluctuations result in density and index-of-refraction fluctuations [5,6]. These fluctuations result in beam jitter (bore-sight error) and higher-order aberrations that reduce the peak irradiance of the laser beam in the far field. Therefore, aero-optical effects can severely limit an airborne directed-energy system's field of regard. To verify wind-tunnel experiments [5] and computational simulations [7–10], aero-optical measurements taken under realistic flight conditions are needed. Yet, to the authors' knowledge, there is no open-literature flight-test data of the flow over a turret available to perform these comparisons. The Airborne Aero-Optics Laboratory (AAOL) [11] reverses this shortfall by adding flight-test capabilities as a viable and affordable experimental tool. This tool not only advances the scientific exploration of aero-optic effects but also allows for real-flight studies of various mitigation schemes involving flow control and adaptive optics.

The AAOL flight program [11] consists of two Citations flying in formation approximately 50 m apart to minimize atmospheric effects. A slowly diverging continuous laser beam approximately 3 mm in diameter is sent from a chase plane to an airborne laboratory; see Fig. 1. The flight-test airborne laboratory consists of a 1-ft-diam (30.5 cm) turret with a 4 in. (10.16 cm) clear aperture; the window can be either flat or conforming to the spherical figure of the turret (i.e., conformal). The turret itself presents a mold line that is a hemisphere on a cylindrical base, which, when installed in the aircraft, protrudes out the side of the Citation through its modified escape hatch. The turret can be extended, so that the cylindrical base protrudes into the airstream by 10.2 cm (which equals the aperture diameter), or withdrawn, so that only the hemisphere protrudes into the airstream. For the data presented in this paper, the turret was configured with a flat window and extended out the door so that 10.2 cm of the cylindrical base protruded into the airstream. At 50 m, the beam from the chase aircraft has diverged to approximately 20 cm so that it

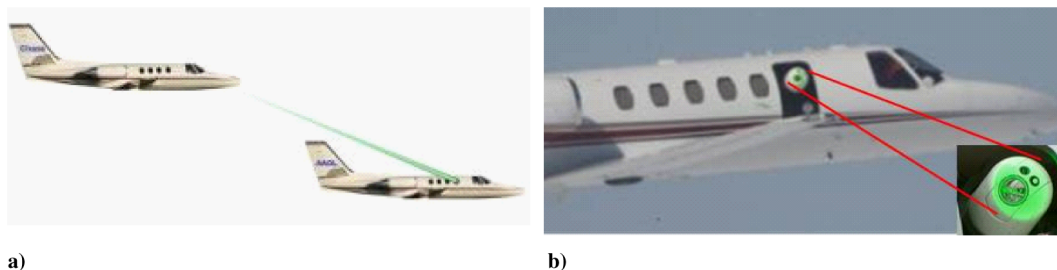


Fig. 1 AAOL: a) two citations flying in formation to measure the aero-optic effects of the flow around a turret, and b) picture of the laser spot on the turret.

overfilled the turret clear aperture by a factor of 2; the diverged beam presents a nominal spherical wave front at the laboratory aircraft-turret pupil, which passes through the aero-optical disturbance and is captured into the turret's beam train. Once the laser and turret systems are tracking each other, a 2.0 cm stabilized beam emerges from the turret mount onto the optical bench in the laboratory aircraft. The spherical figure of the beam due to the divergence from the chase aircraft is removed from the otherwise aero-optically aberrated beam. The "stabilization" of the beam is performed by a closed-loop fast-steering-mirror system that reimaging the turret pupil and is able to reduce the beam's overall jitter to a cutoff frequency of approximately 200 Hz, thus acting as a high-pass jitter filter. The "stabilized beam" is then split to the various sensors on the optical bench onboard the laboratory aircraft. Details of the experimental setup will be discussed later in this paper.

Given the complexity of both the flowfield and experimental setup to measure the aero-optic effects around an optical turret, many fundamental studies have been performed by concentrating on the predominant flow features surrounding a turret, such as separated shear layers [12–15] and turbulent boundary layers [16–19]. Experimental optical data on flat-windowed turrets is limited [5]; to obtain relevant optical data requires facilities large enough for pertinent Reynolds and Mach number flows with optical access. Structural interference from wind tunnels with these capabilities still limits the achievable azimuth and elevation angles where optical data can be acquired. As such, the AAOL also provides a unique capability for obtaining not only flight data but also ranges of azimuth and elevation angles not obtainable in tunnels due to tunnel blockage and interference effects. Although the Mach number limit for the Citations is approximately 0.7, because the flow becomes sonic over the fully protruding turret at flight Mach numbers above 0.55, the AAOL also provides the opportunity of investigating the transonic regime that would require the use of less-available tunnels with difficult installation requirements. This paper covers data up to only Mach 0.5; some results of transonic testing can be found in [20,21].

As we have mentioned, the flow around hemisphere-on-cylinder turrets is complicated; the flow characteristics and their relationship to aero-optic effects are covered in Sec. II. The experimental setups for the flight and tunnel tests are discussed in Sec. III. Section IV presents the optical results from several flights, verifies previously proposed scaling relationships, and presents complementary wind-tunnel results. The conclusions are discussed in Sec. V.

The flow around a hemisphere-on-cylinder turret is highly complex and three-dimensional [5,22]. The dynamics of the flowfield depend upon both the Reynolds number and the Mach number. Still, a few general flow features are apparent for most Reynolds number and fully subsonic Mach number tests (fully subsonic in the sense that the flow is subsonic everywhere over the turret). A full description of the current understanding of the wake region around the turret based on different tunnel experiments and computational-fluid-dynamics simulations is presented in a recent review paper [5] and illustrated in Fig. 2.

At the front of the turret, a necklace vortex forms near the base, extends along the sides of the turret, and continues in the downstream direction aft of the turret. On the upstream half of the turret, the flow remains attached, and an inviscid approximation provides a fair description of that portion of the flowfield; however, there is still an

unsteady component that deviates from the inviscid-flow approximation that is due to unsteadiness introduced on the flow by the necklace vortex. That flow, which is not swept up into the necklace vortex, although somewhat unsteady due to the presence of the necklace vortex, is forced to accelerate as it goes around and over the turret with a favorable pressure gradient on the upstream half of the turret. At the end of the upstream portion and at the aft portion of the turret, the flow experiences an adverse pressure gradient and separates at some point. The location of the separation point and the downstream wake characteristics are dependent on the Reynolds number. As the flow separates, creating a shear layer, coherent vortical structures form and eventually roll up into two large "horn" vortices. The low pressure and associated low density inside these vortical structures result in a spatially and temporally varying index-of-refraction field, thus creating a highly aberrating optical environment.

Depending on the elevation and azimuthal angle, the beam entering or exiting the pupil of the turret propagates through some of these different regions of the flowfield; see Fig. 2. The location of the pupil is most commonly described using azimuth A_z and elevation El angles; however, from a flow-physics point of view, it is more convenient to introduce a different coordinate system to describe the beam direction. This coordinate system uses the viewing angle α and the modified elevation angle β to define the direction of the beam; see Fig. 3. The viewing angle α is defined as the angle between the flow-direction and beam-direction vectors. The modified elevation angle

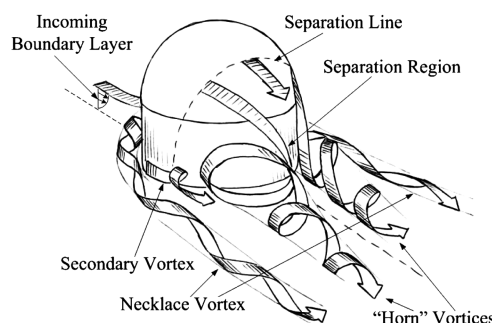


Fig. 2 Schematic of the subsonic flow around a turret [5].

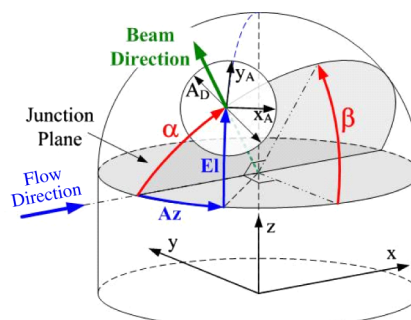


Fig. 3 Definition of angles to describe the beam direction and turret-and aperture-based system of coordinates.

β is defined as the angle between the junction plane joining the hemisphere to the cylinder and the plane formed by the flow-direction and the beam-direction vectors; notice in Fig. 3 that the junction plane is parallel to the surface on which the cylindrical base is attached. These angles are related to the azimuth and elevation angles through the following relations:

$$\alpha = \cos^{-1}(\cos(Az) \cos(EI)) \quad \beta = \tan^{-1}(\tan(EI) / \sin(Az)) \quad (1)$$

The physical reasoning for this coordinate system is based on the observation that, for flow around a sphere, the time-averaged flow quantities are a function of the viewing angle α only. The addition of the modified elevation angle β accounts for the presence of the cylindrical portion of the turret, the presence of the surface on which the turret is mounted, and the location of the horn vortices; in the remainder of this paper, effects associated with β will be referred to as mounting-base or surface-plane effects. The effect of the flat-window at the turret pupil on the asymmetry of the flowfield will also be seen in the modified elevation angle.

It is also convenient to introduce two systems of coordinates: one for the turret and another for the aperture. For the turret-based system of coordinates (x, y, z) , the x axis is chosen to be parallel with the flow direction, the z direction is along the turret vertical axis, and the y axis is orthogonal to both the x and z axes; see Fig. 3. The aperture-based system of coordinates (x_A, y_A) ; see Fig. 3) has the x_A axis parallel to the junction plane, and the y_A axis is orthogonal to it pointing upward.

As mentioned previously, the unsteady wake generated by the flow around the hemisphere-on-cylinder turret results in pressure, temperature, and density fluctuations. Through the Gladstone–Dale constant K_{GD} , the density ρ and the index-of-refraction n are related by

$$n(x, y, z, t) - 1 = K_{GD}\rho(x, y, z, t) \quad (2)$$

Given a variable refractive index flowfield, an initially collimated, planar wavefront laser beam that propagates through the flowfield emerges with an aberrated wave front. A wave front is defined as a surface of constant phase; if the mean phase is removed, then the wave front is described by a surface of constant phase error (from the mean); that surface is displaced from the mean by a distance above and below the line of constant mean phase. It can be shown mathematically that the magnitude of the distance above and below the line of constant phase is equal to the magnitude of the surface defined by the optical path difference (OPD); the two are, in fact, conjugates of one another. If we assume that the propagation direction is in the z direction, then the OPD is calculated by first obtaining the optical path length (OPL), which is calculated as

$$OPL(x, y, t) = \int_{s_1}^{s_2} n(x, y, z) dz \quad (3)$$

from which the OPD is found by

$$OPD(x, y, t) = OPL(x, y, t) - \langle OPL(x, y, t) \rangle \quad (4)$$

where angled brackets represent the spatially averaged optical path length over the aperture, x, y , at a given time, t .

II. Flight Experiments

As described in the introduction, a flight experiment consisted of a laser source aircraft and the main, data-acquisition laboratory aircraft. The data-acquisition aircraft (the AAOL itself) had both the protruding turret and the instrumentation for characterizing the aero-optic effects associated with the turret's azimuth and elevation angles. Once in formation at the proper distance and the desired azimuth and elevation with respect to the turret, the laser source aircraft irradiated the turret pupil, causing the beam to pass through the aero-optical flow and enter (in this case, the turret's flat-window; Fig. 4). The beam reflected off the primary and secondary mirrors, which contracted the beam and directed it into the Coude path, where a second telescope removed the nominal spherical curvature. The overall contraction took the beam from the clear aperture of 10.2 cm in diameter to the bench where it was now 2.0 cm in diameter. The beam was then reflected off the fast steering mirror (FSM) to remove overall jitter and onto the optical bench. The beam was then split by a beam splitter into two beams; see Fig. 5. One beam was sent to a position-sensing device (PSD), which measured the residual jitter in the beam after the FSM. Also, the signal from this PSD was used in a closed-loop control FSM system, which stabilized the outgoing beam for frequencies up to 200 Hz, as vibration measurements of the optical table in flight did not reveal any significant frequency content above 100 Hz.

The second beam was transmitted toward a high-speed Shack–Hartmann wave front sensor (WFS) through a set of relay optics to reimagine the turret pupil onto the lenslet; see Fig. 5. The Shack–Hartmann sensor used for these tests can be operated at capture rates up to 100 kHz, with the maximum framing rate depending on the number of charge-coupled device (CCD) pixels interrogated, which in turn affects the number of subapertures that can be used on the sensors lenslet array. The full CCD array would allow for a spatial resolution of 60×71 lenslets with a maximum capture rate of 7 kHz; on the other hand, if 32×32 lenslets were used, the wave fronts could be captured at up to 20 kHz. For the majority of the tests, 32×32 lenslets framed at 20 kHz were used for the fixed-angle data, and 32×32 lenslets framed at 3 kHz were used for the slew data. To minimize spatial smearing, the camera's integration time was set at $0.5 \mu s$. For the results presented in this paper, from each of the wave-front datasets, the mean aberration from the time series (referred to as steady-lensing aberration) was removed, as well as the instantaneous (i.e., for every frame) piston and tip/tilt (i.e., the residual jitter not removed by the FSM) leaving only higher-order aberrations.

In addition to the high-speed wave-front measurements, Fig. 5 also shows the schematic of additional measurements made during flights. The instantaneous azimuth and elevation angles of the turret were recorded simultaneously with aero-optical measurements. Also, a boundary-layer Pitot rake was installed below the turret; see Fig. 4, left picture, from which the total and static pressures of the freestream were collected to calculate the freestream Mach number using isentropic compressible relation. The boundary-layer thickness was also measured by the Pitot probe rake to be approximately 50 mm.

All wave-front measurements referred to here were collected at an altitude of 15,000 ft for Mach numbers of either 0.4 or 0.5. Wave-front data for this paper were collected for two flight modes, the first with the two aircraft fixed in their relative positions to one another,



Fig. 4 Photographs of the turret mounted on the Citation with a schematic of the turret assembly and shell of the aircraft.

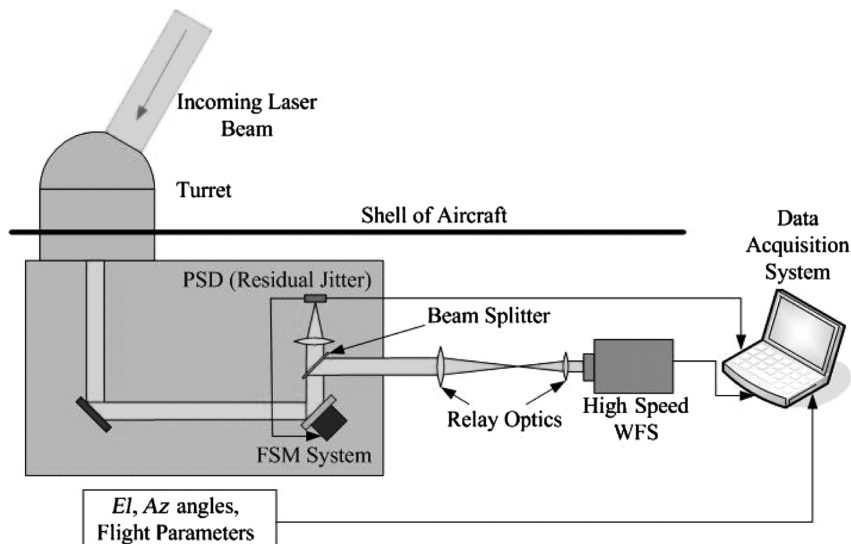


Fig. 5 Optical setup of the beam path and suite of instruments during flight tests.

which fixed the azimuth and elevation angles (later called fixed-angle data), or with one aircraft passed by the other, which caused the data to have a time-varying azimuth and elevation angles, later referred to as slewing data. For the fixed angle, the wave-front sensor acquired data at the 20 kHz frame rate for 0.5 s (10,000 wave fronts).

For the slewing data, the frame rate of the camera was reduced to 3 kHz, and the sampling time was increased to 14 s; this allowed the rapid collection of wave fronts over a range of viewing angles to obtain reliable wave-front statistics, like time-averaged OPD_{RMS} , etc., at these viewing angles. During this time interval, the laser source aircraft reduced its speed, allowing the laboratory aircraft to slowly pass the source aircraft so that the azimuth/elevation angles between the two planes slowly and monotonically changed. An example of the time record of the azimuth/elevation angles during a slewing maneuver is shown in Fig. 6. The elevation angle during this maneuver remained nearly constant, while the azimuth angle and thus the viewing angle increased almost monotonically by 15–20 deg. During each slewing maneuver, 42,000 wave fronts were recorded. For the analysis, each dataset was split into sequential subsets of 3,000 wave fronts (1 s subsets). For each subset, the time-averaged wave front and the instantaneous tip/tilt were removed, and the spatial statistics, such as the time-averaged spatial OPD_{RMS} , were calculated. For each 1 s subset, the corresponding time-averaged azimuth and elevation angles of the flat-windowed aperture were recorded. A total of 15 slewing maneuvers were performed during reported flight tests.

Typical flow time scales around a turret at these Reynolds and Mach numbers were on the order of a few milliseconds, while the angular rate of rotation of the turret during a slewing maneuver was on the order of a degree per second. Therefore, at every moment, the

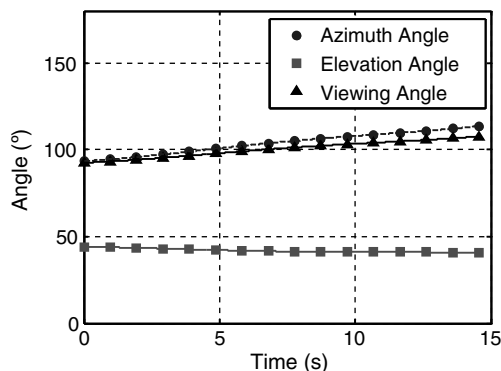


Fig. 6 Example of the instantaneous azimuth, elevation, and viewing angles of the turret during a slewing maneuver.

flow quickly adjusted to the slow-changing aperture location, and the optical statistics (i.e., time-averaged OPD_{RMS}) were not affected by the rotation of the turret; thus, the slewing maneuvers allowed for a rapid mapping of the aero-optic environment around the turret, yielding a large amount of statistical data over a range of azimuth and elevation angles. To verify that the rotation of the turret during the data-acquisition process did not influence the optical statistics, Fig. 7 shows the convergence of the mean spatial OPD_{RMS} of a fixed-angle dataset and the corresponding subset of a slewing maneuver at the same azimuth/elevation angles. Only a small 1% difference exists between the converged mean of the fixed-angle test and subset of the slewing maneuver; similar results were observed for other data sets investigated. Therefore, statistically breaking up the slewing data into small subsets of data is equivalent to acquiring a series of time-uncorrelated fixed-angle data points. Furthermore, higher-order statistics, up to the fourth moment, were calculated and were found to be very similar between fixed-angle and slewing subsets. Therefore, unless mentioned otherwise, no distinction will be made between the fixed-angle and slewing-maneuver data.

In addition to the flight tests, aero-optical measurements around the same turret were performed in the University of Notre Dame's 0.9×0.9 m wind tunnel to compare the tunnel data with the flight data. The wind tunnel is a closed-loop, temperature-controlled wind tunnel, capable of freestream Mach numbers up to 0.67 with no models in the tunnel, and it has a turbulent intensity below 0.05% [23]. For the tunnel tests, the freestream Mach number was 0.3. The turret assembly was tilted and placed under the test section in such a way that the turret was protruded normally through the bottom test section wall by the same amount as in flight. The boundary-layer thickness was 30 mm upstream of the turret, which is similar with the

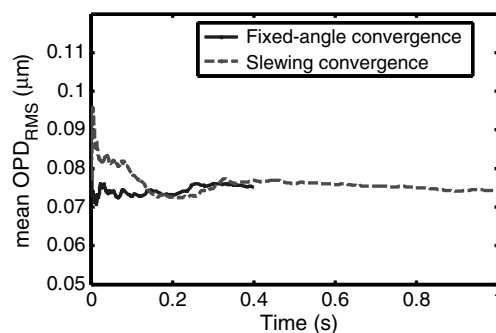


Fig. 7 Convergence of the mean spatial OPD_{RMS} of a fixed-angle test and the 1 s subset of a slewing maneuver corresponding to the same azimuth and elevation angles.

boundary-layer thickness of 50 mm in flight. The experimental setup and pictures of the turret installed in the test section are presented in Fig. 8. The slowly diverging laser beam traveled approximately 50 m, matching the distance between planes in flight, before it was forwarded to the turret aperture. The turret was actively tracking the beam, so that the steering mirror was moved to different positions to achieve a range of elevation angle between 40 and 50 deg and a range of azimuthal angles between 90 and 130 deg. After exiting the turret assembly, the beam was contracted and forwarded to the high-speed sensor the same way as it is done in flights; see Fig. 5.

III. Results

A. Flight Data

To gain a better understanding of the aero-optic environment around the flat-windowed turret, time-averaged spatial variations of aero-optical distortions OPD_{RMS} over a large range of azimuth and elevation angles were measured and presented in Fig. 9. In addition, Fig. 9a shows the locations of all the elevation/azimuth points (light dots) where aero-optical distortions were measured. Figure 9b shows the same data points as a function of the viewing and modified-elevation angles; Figs. 9c and 9d show the data as a location of the aperture center on the surface of the turret, flow direction is along x axis. In all these figures, the normalized spatial OPD_{RMS} ,

$$OPD_{Norm}(\mu\text{m}/\text{m}) = \frac{OPD_{RMS}}{(\rho_0/\rho_{SL})M^2D} \quad (5)$$

was calculated, and the data in between points were linearly re-interpolated between the closest neighbors to create a continuous surface to fill in the appropriate gaps. Note that the units of the normalized OPD_{RMS} are microns per meters. Analysis of experimental error showed that experimental error was approximately

$0.2 \mu\text{m}/\text{m}$, mostly independent of the elevation/azimuthal angles. For clarity, experimental error bars will not be plotted in related figures.

Analyzing the results in Fig. 9, at forward-looking angles, $Az < 70$ deg or $\alpha < 70$ deg, the normalized OPD_{RMS} remained around 1, which was comparable with the sensitivity of the wave-front sensor. This indicates that the aero-optic environment at these angles was not largely affected by higher-order aero-optic aberrations. However, beyond an azimuth (or viewing) angle of 70 deg, the normalized OPD_{RMS} began to increase, reaching a local maximum between 2 and 2.5 at approximately 90 deg. As shown in Fig. 9b, the normalized OPD_{RMS} was only a weak function of the modified elevation angle β for viewing angles below 90 deg. The location of the first peak in the normalized OPD_{RMS} changed by only a few degrees within a range of all modified elevation angles tested; however, in the azimuth/elevation angle space, the azimuth location of the first peak changed by roughly 20 deg over tested elevation angles. This illustrates the usefulness of the viewing-angle space, defined in Fig. 3, and indicates that mounting-base (or surface-plane) effects over this range of angles are minimal. After this first peak in the normalized OPD_{RMS} , as the viewing angle continued to increase, the normalized OPD_{RMS} began to drop slightly; this phenomenon was attributed to tip/tilt-removal effects and is discussed in detail in [24,25].

Figures 10a and 10b examine surface-plane effects in more detail. These are the same data as those presented in Fig. 9, but they are plotted for various modified elevation-angle regions. In Fig. 10a, it can be seen that, for forward-looking angles, the normalized OPD_{RMS} is largely unaffected by surface-plane effects (i.e., modified elevation-angle effects), although the location of the first peak (for α from 90 to 100 deg) shifted slightly as a function of the modified elevation angle. The origin of this peak was discussed in the previous section. As the viewing angle continued to increase toward 120 deg, the beam propagated through a larger portion of the

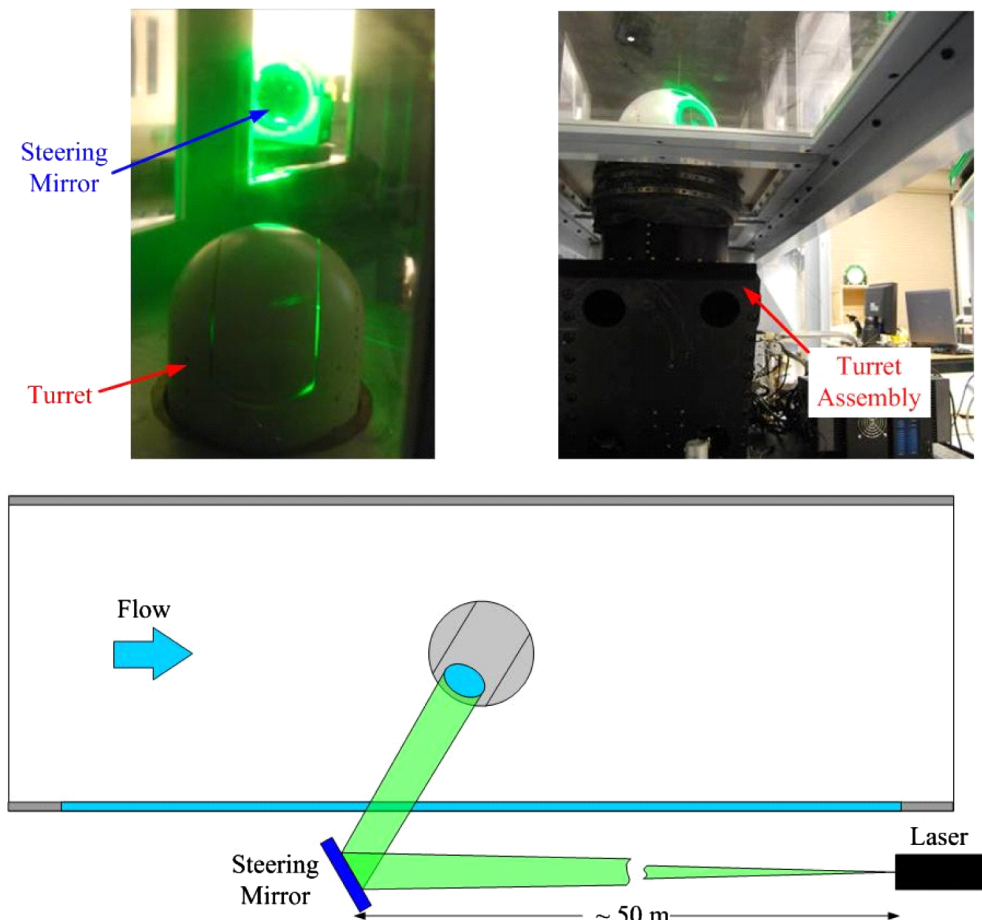


Fig. 8 Turret assembly installed in the tunnel: pictures (top) and experimental setup (bottom).

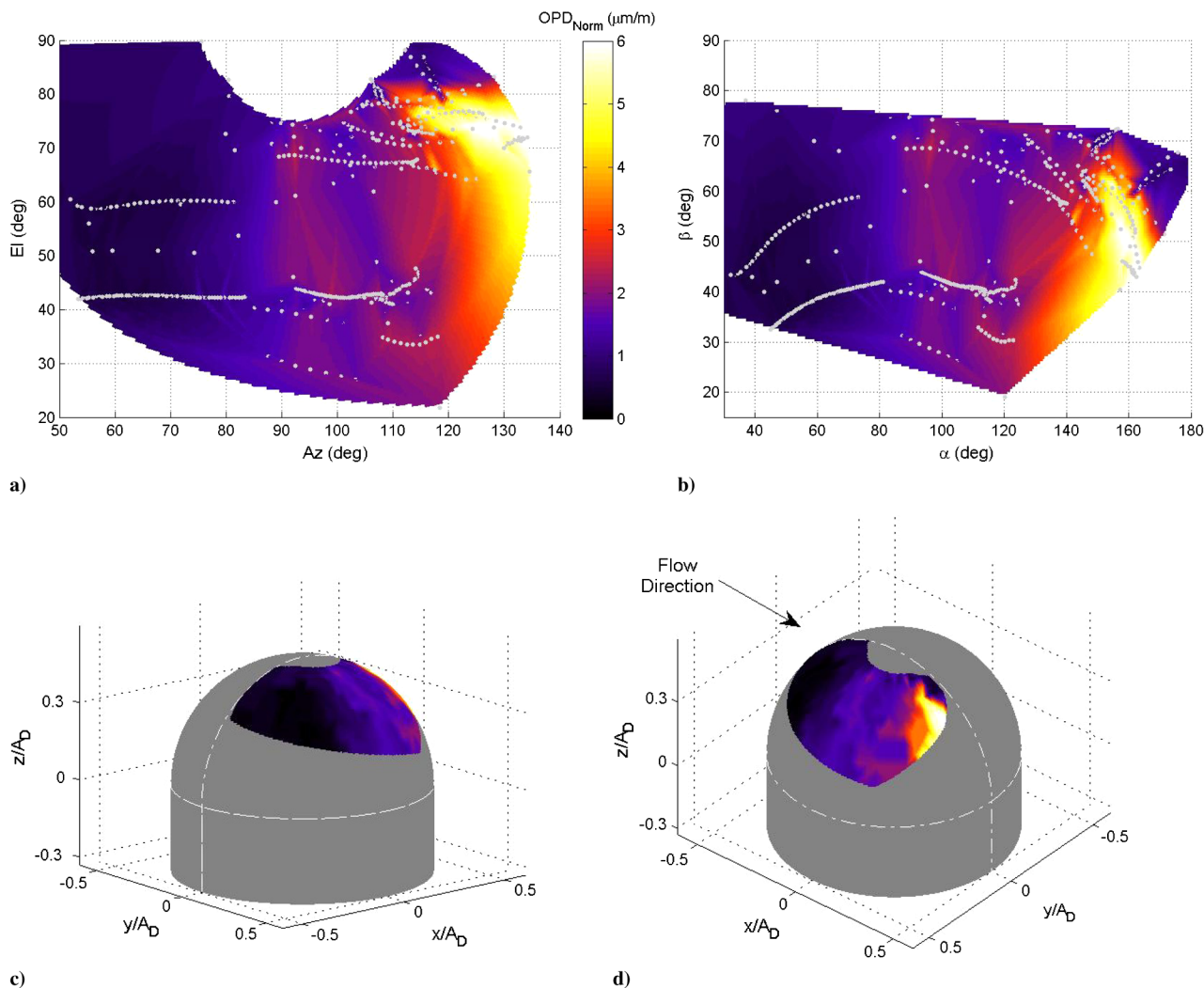


Fig. 9 Time-averaged OPD_{RMS} as a function of a) $EI - Az$ angles, b) $\alpha - \beta$ angles, c) and d) as the location of the aperture center on the turret.

wake. Simultaneously, the vortical structures in the wake grew larger in this region of the wake, and the normalized OPD_{RMS} increased rapidly, more than doubling over a few degrees. The data in Fig. 10a represent the data for modified elevation angles from 20 to 80 deg. The data from Fig. 10a have been represented by a single curve in Fig. 10b, with the error bars showing not the experimental errors but rather the data variation over all modified elevation angles in Fig. 10a; however, additional data for modified elevation angles greater than 80 deg have been added to Fig. 10b. As can be seen in Fig. 10b, above a viewing angle of 100 deg, the data show a marked departure from Fig. 10a.

Figures 10a and 10b, taken together, allow for a closer analysis of the deviation from the data collapse simply on viewing angle. As pointed out previously, the location of the first local maximum around the viewing angle of 90 deg is dependent upon the modified elevation angle, implying that the location of the maximum is sensitive to surface-plane effects. More importantly, for modified elevation angles less than 80 deg, the normalized OPD_{RMS} approaches a value of nearly 6 around the viewing angle of 130 deg; however, for a modified elevation angle greater than 80 deg, the normalized OPD_{RMS} dropped to a value of 2, demonstrating that a “sweet spot” exists in the zenith plane that is clearly not present for modified elevation angles just 10 deg away from zenith. Computational simulations [26,27] have shown that, in this region near the centerline of the turret (i.e., in the zenith plane), associated with an azimuth angle of 180 deg, the beam propagates through a relatively quiet region of the wake traveling in between the two horn vortices, as depicted in Fig. 3. This is consistent with centerline measurements on

a canonical flat-windowed turret [28], along with conformal-window turret tests [5], where normalized levels of aero-optical distortions were also around a value of 2.

Returning to the modified elevation-angle data for $\beta < 80$ deg, it is useful to examine the time-averaged and instantaneous wave fronts; Fig. 11 shows the spatial distribution of the wave-front temporal variance for data in the region between $60 < \beta < 70$ deg. Figure 11 shows temporal variance of the normalized OPD, $(\overline{[OPD_{Norm}(x, y, t)]^2})^{1/2}$, where the overbar indicates the temporal averaging, at every spatial point across the aperture for viewing angles of 81, 92, 99, and 117 deg along with the time-averaged OPD_{RMS} over the entire aperture. The flow across the aperture is from left to right. Notice that the temporal variances of the normalized OPD across the aperture are not constant. Except for the 81 deg case, the magnitude of the fluctuations in the upstream portion of the aperture is smaller than the magnitude of the fluctuations in the downstream portion of the aperture. This indicates that, as the flow separates from the turret at back-looking angles, the aero-optical structures grow as they propagate downstream, and so any wave-front measurements based on the frozen flow hypothesis, like the Malley probe [28], should be treated with caution.

Figure 12 shows a selected instantaneous wavefront corresponding to each of the four selected wavefront temporal variation data sets shown in Fig. 11, flow goes from left to right. In Fig. 12, the scaling in each graph has been adjusted to aid in viewing aberrations in the wave front. For example, the aberrations shown in Fig. 12a are only half as large as the aberrations shown in Figs. 12b and 12d. Notice, in Fig. 12a, that the size of the aberrations, relative to

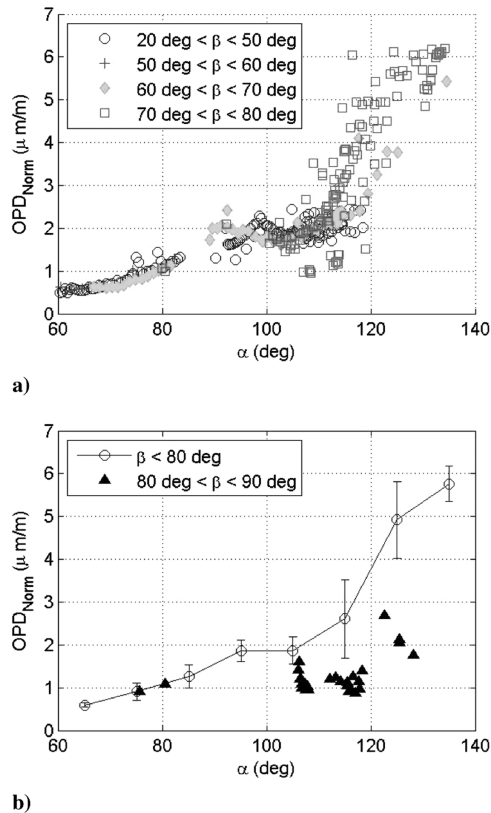


Fig. 10 Changes in the normalized OPD as a function of viewing angle for different elevation angle ranges. Bars denote the variation of data over all modified elevation angles and not experimental error.

the aperture, are smaller and less coherent than the structures seen at the backward-looking angles. In the wave fronts at backward-looking angles, the aberrations appeared as long spanwise-coherent structures resulting from the coherent vortical structures in the shear layer forming as the flow separates over the front portion of the aperture. Additionally, in Fig. 12b, which corresponds to the first peak in the normalized OPD_{RMS} , the upstream portion of the aperture had a local separation bubble that formed from the slope-discontinuity of the flat-windowed aperture [24,25]. The evidence of this unsteady bubble can also be seen in the spatial distribution plot in Fig. 11 for the viewing angle of 91 deg.

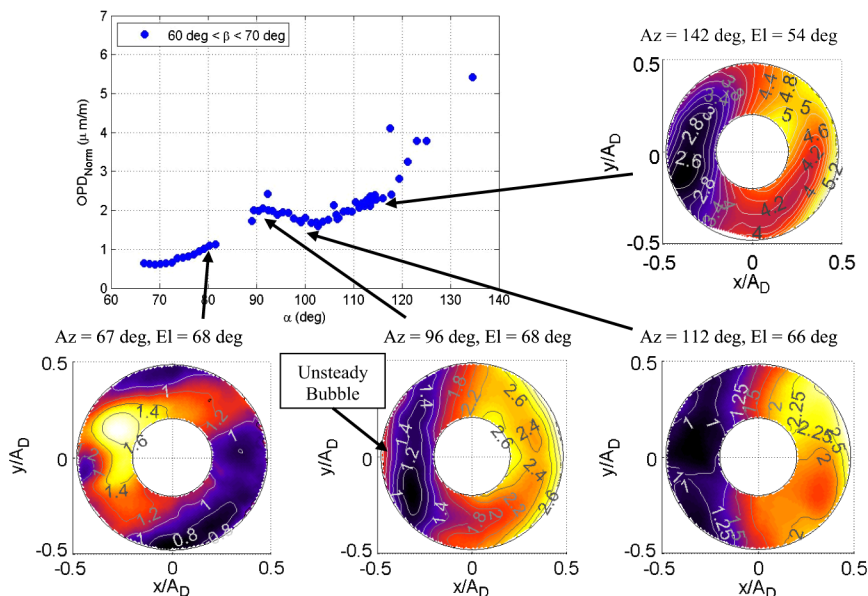


Fig. 11 OPD_{Norm} centered between $60 < \beta < 70$ deg with spatial distributions of the wavefront temporal variance across the aperture for selected angles. Color scales are different for each subplot.

B. Mach Number Dependence

For the data presented previously, all of the data were normalized by a scaling factor of $(\rho_0/\rho_{SL})M^2D$. To verify that, at subsonic Mach numbers, this scaling relationship successfully collapsed the data, flight tests were performed at Mach numbers of 0.4 and 0.5. The data were acquired at 15,000 ft to assure that the only change in the scaling relationship was the Mach number. Figure 13 shows two data sets on each plot: one at Mach 0.4 and the other at Mach 0.5. Both data sets were acquired over an azimuth angle range of 145–160 deg and an elevation angle range of 45–67 deg during their respective slewing maneuvers, so that surface-plane and flat-window effects were identical between the two data sets. The top graph shows the unscaled data, in which the magnitude of the aberration at Mach 0.5 is larger than the magnitude of the aberration at Mach 0.4. As shown in the bottom graph, the data successfully collapse onto a single curve when scaled by $(\rho_0/\rho_{SL})M^2D$, verifying the proposed scaling relationship.

Also in Fig. 13, the temporal variation of OPD_{RMS} , defined as $\sqrt{(OPD_{RMS}(t) - \overline{OPD_{RMS}})^2}$, is presented for different viewing angles as bars. Note that this is not experimental error but a variation of OPD_{RMS} in time. This temporal variation leads to the time-changing far-field intensity, which might impact free-space, laser-based communication systems [20,29].

C. Tunnel Data

Figure 14 shows the comparison between wind-tunnel tests and flight tests at comparable range of angles. For both the flight and tunnel tests, the Reynolds number based on turret diameter was approximately 2 million, which is well above the laminar-to-turbulent transition range of $Re_D = 300,000$ [5]. Both the tunnel and flight data were normalized by $(\rho_0/\rho_{SL})M^2D$.

As shown in Fig. 14, the normalization of the data collapses both the tunnel and the flight data to similar nominal values. The viewing angle of the first local maximum, corresponding to the presence of the unsteady separation bubble at the leading edge of the flat aperture, has shifted from approximately 102 deg for the flight data to a larger value of 108 deg in the tunnel tests. The reason for the shift in the peak is currently being investigated, but it is probably related to the boundary layer separating from the turret earlier during flight than in the tunnel because of tunnel-blockage effects. In the 0.9×0.9 m tunnel, the turret has a blockage of $\sim 7\%$, where we here hypothesize that it has changed the separation by ~ 6 deg; however, in testing a turret with an even larger tunnel blockage, it was observed that the blockage has delayed separation up to 130 deg [5]. Given the difference in the elevation angle and blockage effects, the normalized

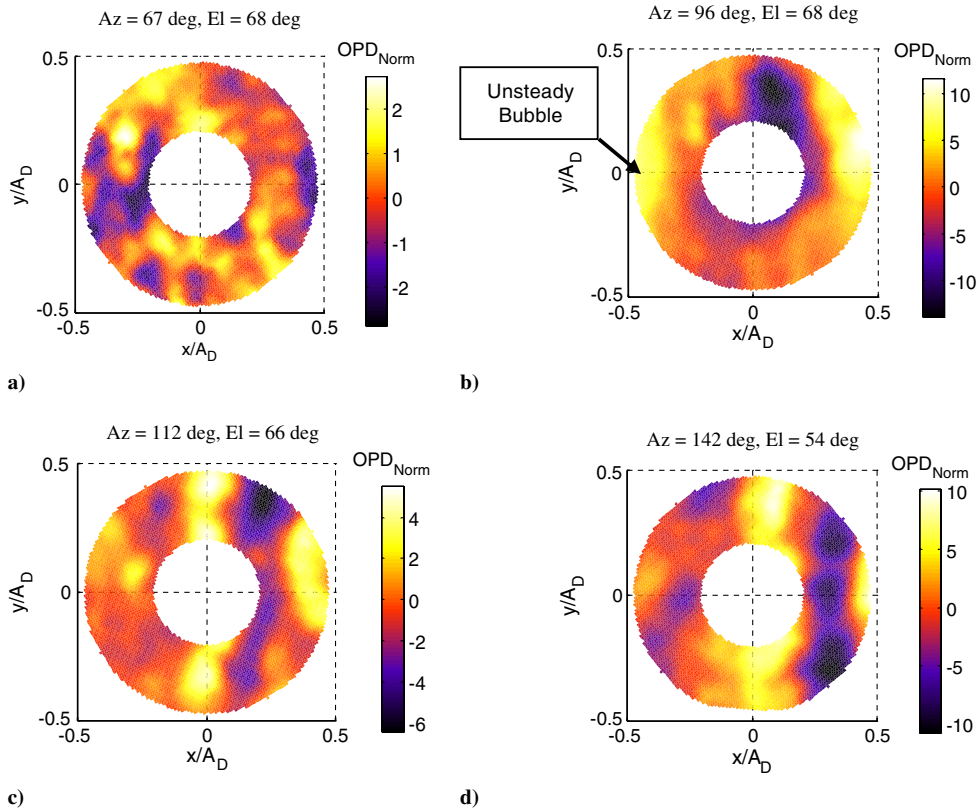


Fig. 12 Instantaneous realizations of wavefronts for a) $\alpha = 81$ deg, b) $\alpha = 92$ deg, c) $\alpha = 99$ deg, and d) $\alpha = 117$ deg. The color map in each part is adjusted appropriately.

data from the tunnel tests and from the flight tests match fairly well, and the existing differences are mostly within the error of the measurements, as the experimental error was estimated to be about $0.2 \mu\text{m}/\text{m}$.

D. Structure Size and Correlation of the Data

Both streamwise and spanwise correlation lengths can be obtained by autocorrelating the wave fronts. Figure 15 shows a normalized-autocorrelation two-dimensional map and the corresponding slices through the correlation map at $\Delta y/A_D = 0$ and $\Delta x/A_D = 0$; the data shown are in-flight data at an azimuth angle of 134 deg and an

elevation angle of 65 deg, which corresponds to a viewing angle of 107 deg. At this viewing angle, the flow separates at the leading slope discontinuity of the flat aperture and forms a spatially evolving shear layer over the aperture [26,28]. Using the definition of the correlation length as the location of the first minima, the structure size in this case was approximately $0.3A_D$. This result is slightly larger than the correlation lengths reported in [28], where the streamwise correlation length was $0.25A_D$, although the Mach number and viewing angle were different in that case; furthermore, one-dimensional wave fronts were measured in [28] using a Malley probe, and so spanwise effects were not captured. Concentrating on the fixed-angle data between $60 < \beta < 70$ deg, the structure size was calculated for the various viewing angles and results are presented in Fig. 16. The structure size, defined as a location of the first minima in the streamwise direction, decreases as the viewing angle increases until it approximately levels out around 93 deg. This location corresponds to the angle at which the normalized OPD_{RMS} reaches the first local maxima at these modified elevation angles. The correlation length starts increasing for large viewing angles above 110 deg, consistent with the fact that the separated region over the aperture and vortical structures inside of it get larger for large viewing angles.

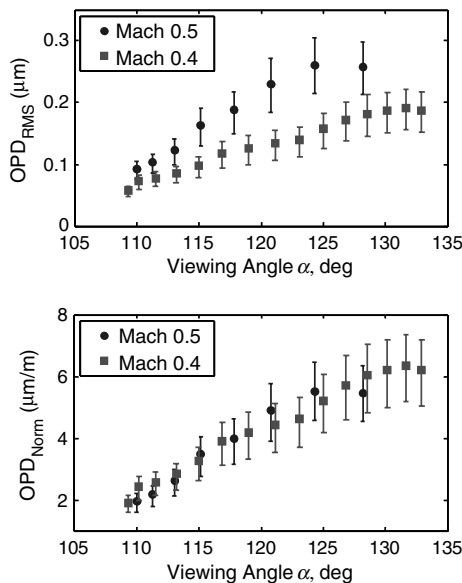


Fig. 13 Comparison of optical data for $M = 0.4$ and 0.5 , the unscaled data (top plot), and the scaled data (bottom plot). Bars indicate levels of temporal variation of OPD_{RMS} .

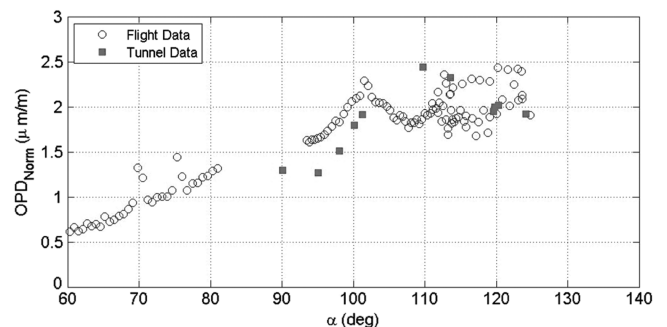


Fig. 14 Comparison of flight data and tunnel data for the AAOL turret for $\beta < 45$ deg. Experimental error is about $0.2 \mu\text{m}/\text{m}$.

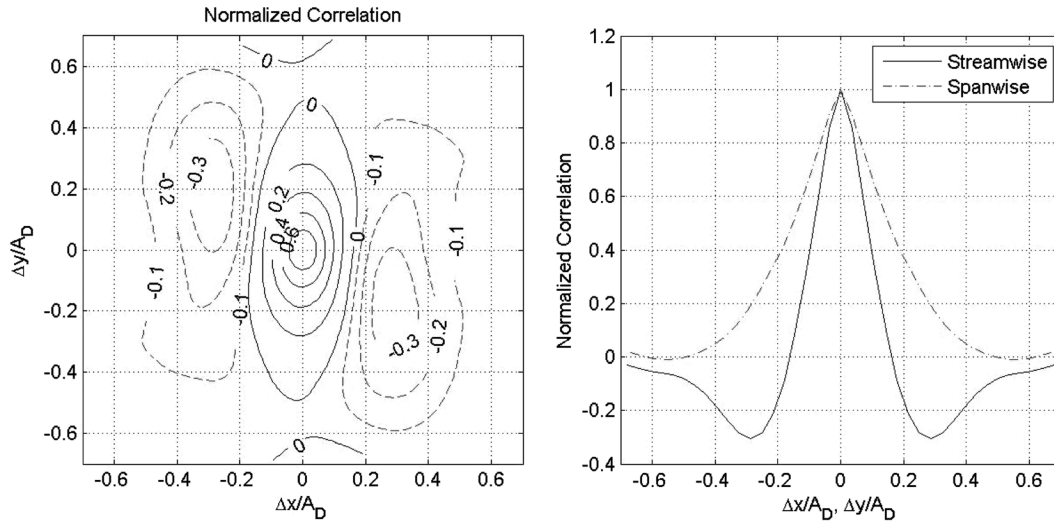


Fig. 15 Normalized autocorrelation of OPD at $Az = 134$ deg, $El = 65$ deg, $\alpha = 107$ deg; incoming $M = 0.5$.

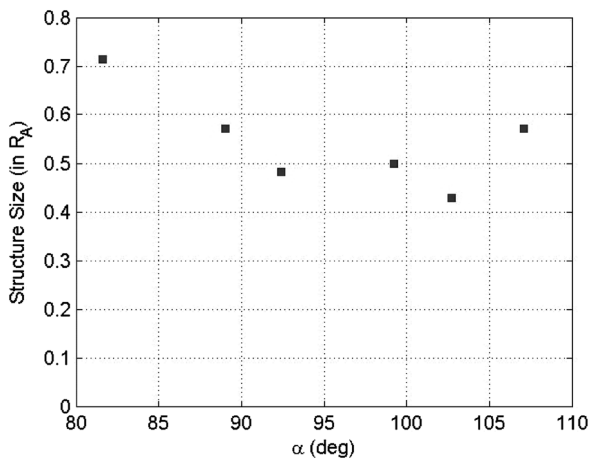


Fig. 16 Calculated structure size from auto correlating wave-front data for $60 < \beta < 70$ deg.

Using the time-resolved wave-front data, the convective velocity of optical structures can be calculated in one of several ways: 1) by spatially cross-correlating time-delayed wave fronts over the entire aperture; 2) by calculating the phase slope as a function of the frequency, similar to the Malley probe analysis [28,30]; 3) by analyzing spatially temporary-resolved wave fronts in the frequency-wavenumber space [31]; or 4) by using other methods. Figure 17 shows the average calculated velocity of the optical structures based on the first approach. Depending on the time difference between the wave fronts being correlated, the optical structure velocity varied slightly; however, for all the cases, the structures were primarily propagating in the streamwise direction

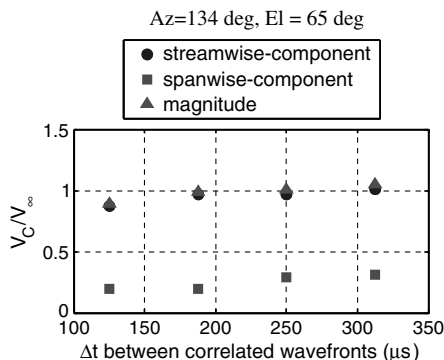


Fig. 17 Calculated velocity by correlating wavefronts using different time delays between wavefronts at a flight speed of Mach 0.5.

across the aperture at a velocity of approximately 0.95 of the freestream velocity. Similar values were reported in [28]. Note that the local flow speed over the aperture is larger than the freestream velocity by approximately a factor of 1.5 due to the fact that the flow naturally accelerates as it passes over the turret; this factor was calculated using static pressure measurements over conformal-window turrets with the same diameter-to-height ratio [5]. As mentioned previously in relationship to Fig. 14, the presence of tunnel walls not only adds to the acceleration over a turret but also affects the flow angularity, which provides the possible explanation for the 6 deg shift in the local peak between 90 and 100 deg in Fig. 14. Taking the 1.5 multiplier of the flow over the top of the turret, the convective velocity of the aberrating structures convecting over the aperture was approximately 0.6 of the local flow velocity over the aperture. This value is consistent with the normalized convective speed of large-scale structures within shear layers and has been observed experimentally at back-looking angles in other tests [24,28].

IV. Conclusions

This paper presents the results of the extensive measurements of the complex aero-optical environment around the side-mounted, flat-window turret performed in-flight using the Airborne Aero-Optics Laboratory (AAOL). Before this set of data, optical-experimental data of the aero-optical environment around a flat-windowed turret in open literature were very sparse, with the largest published data set consisting of only four data points. Furthermore, all data up to this point have been obtained either in a wind tunnel or computationally. The AAOL provides a unique capability to collect large amounts of flight data during relatively short flight sequences. Using a high-speed wave-front sensor onboard the AAOL allows acquiring wave fronts at different azimuth/elevation angles with good spatial and temporal resolution. To analyze the data, a different frame of reference, the viewing and modified-elevation angles, was proposed. In this frame of reference, differences in optical data at a fixed viewing angle can be directly attributed to surface-plane effects and asymmetries in the wake around the turret. Results showed that aero-optical aberrations are negligible for small forward-looking viewing angles less than 70 deg, where aero-optical effects are primarily from a less-aberrating attached boundary layer over the turret. Above 70 deg, a small separation bubble appeared at the front edge of the flat window, introducing convecting, small-scale structures over the aperture and causing aero-optical distortions to increase. The separation bubble increases with the increased viewing angle, leading to a subsequent increase in aero-optical distortions. The aero-optical levels have a local peak around the viewing angle between 90 and 100 deg, followed by a small drop in the levels in the range of viewing angles between 100 and 110 deg. This drop in the aero-optical

distortions, also observed in other experiments, was contributed to the fact that the instantaneous tip-tilt was removed from aero-optical data. Above 110 deg, aero-optical aberrations increase sharply with the viewing angle as the laser beam propagates through a stronger region of the turbulent wake, dominated by unsteady horn vortices. These increased aero-optical levels were not observed for the region aft of the turret near the center plane with the azimuth angle around 180 deg, where the levels stayed approximately constant or even decreased, as the flow in this region between horn vortices is relatively quiet.

Data sets in flight at different Mach numbers showed that the scaling relationship normalizing low subsonic optical data by $(\rho_0/\rho_{SL})M^2D$ successfully captured the Mach number dependence. In addition to time-averaged levels of aero-optical distortions, cross-correlation maps and mean convective speeds were calculated at selected angles; results were found to agree favorably with previously reported measurements. Finally, flight results were compared to wind-tunnel data results and differences were discussed.

Acknowledgments

The authors would like to thank the Northern Air personnel, especially Kevin Tessmer for providing technical assistance during flight test. We would also like to thank Matthew Krizo from the Air Force Institute of Technology (AFIT) for providing assistance on the laser tracking system.

These efforts were sponsored by the High Energy Laser Division of the Joint Technology Office and supported by the U.S. Air Force Office of Scientific Research, grant FA9550-07-1-0574.

References

- [1] Duffner, R., *The Adaptive Optics Revolution: A History*, Univ. of New Mexico Press, Albuquerque, NM, 2009, pp. 202–235.
- [2] Ross, T. S., “Limitations and Applicability of the Maréchal Approximation,” *Applied Optics*, Vol. 48, No. 10, 2009, pp. 1812–1818. doi:10.1364/AO.48.001812
- [3] Butts, R., and Weaver, L. D., “Airborne Laser Experiment (ABLEX): Theory and Simulations,” *Proceedings of SPIE 2120, Laser Beam Propagation and Control*, Vol. 10, Los Angeles, CA, June 1994.
- [4] Weaver, L. D., and Butts, R., “ABLEX: High Altitude Laser Propagation Experiment,” *Proceedings of SPIE 2120, Laser Beam Propagation and Control*, Vol. 30, Los Angeles, CA, June 1994.
- [5] Gordeyev, S., and Jumper, E. J., “Fluid Dynamics and Aero-Optics of Turrets,” *Progress in Aerospace Sciences*, Vol. 46, No. 8, 2010, pp. 388–400. doi:10.1016/j.paerosci.2010.06.001
- [6] Wang, M., Mani, A., and Gordeyev, S., “Physics and Computation of Aero-Optics,” *Annual Review of Fluid Mechanics*, Vol. 44, Jan. 2012, pp. 299–321. doi:10.1146/annurev-fluid-120710-101152
- [7] Ladd, J., Mani, M., and Bower, W., “Validation of Aerodynamic and Optical Computations for the Flow About a Cylindrical/Hemispherical Turret,” *27th AIAA Applied Aerodynamics Conference*, AIAA Paper 2009-4118, June 2009.
- [8] Pond, J. E., and Sutton, G., “Aero-Optic Performance of an Aircraft Forward-Facing Optical Turret,” *Journal of Aircraft*, Vol. 43, No. 3, 2006, pp. 600–607. doi:10.2514/1.18601
- [9] Morgan, P. E., and Visbal, M. R., “Large Eddy Simulation of Flow Over a Flat-Window Cylindrical Turret with Passive Flow Control,” *48th AIAA Aerospace Sciences Meeting*, AIAA Paper 2010-916, Jan. 2010.
- [10] White, M. D., Morgan, P. E., and Visbal, M. R., “High Fidelity Aero-Optical Analysis,” *48th AIAA Aerospace Sciences Meeting*, AIAA Paper 2010-433, Jan. 2010.
- [11] Jumper, E., Zenk, M., Gordeyev, S., and Cavalieri, D., “The Airborne Aero-Optics Laboratory, AAO,” *Proceedings of SPIE*, Vol. 8395, Paper :8395-6, June 2012.
- [12] Fitzgerald, E. J., and Jumper, E. J., “The Optical Distortion Mechanism in a Nearly Incompressible Free Shear Layer,” *Journal of Fluid Mechanics*, Vol. 512, Aug. 2004, pp. 153–189. doi:10.1017/S0022112004009553
- [13] Rennie, R. M., Duffin, D. A., and Jumper, E. J., “Characterization and Aero-Optic Correction of a Forced Two-Dimensional Weakly Compressible Shear Layer,” *AIAA Journal*, Vol. 46, No. 11, 2008, pp. 2787–2795. doi:10.2514/1.35290
- [14] Zubair, F. R., Freeman, A. P., Piatrovich, S., Shockro, J., Ibrahim, Y. N., and Catrakis, H. J., “Large Scale Turbulence Suppression Control for Direct Reduction of Aero-Optical Aberrations,” *38th AIAA Plasmadynamics and Lasers Conference*, AIAA Paper 2007-4008, June 2007.
- [15] Catrakis, H. J., and Aguirre, R. C., “New Interfacial Fluid Thickness Approach in Aero-Optics with Applications to Compressible Turbulence,” *AIAA Journal*, Vol. 42, No. 10, 2004, pp. 1973–1981. doi:10.2514/1.547
- [16] Cress, J. A., Gordeyev, S., Post, M. L., and Jumper, E. J., “Aero-Optical Measurements in a Turbulent, Subsonic Boundary Layer at Different Elevation Angles,” *39th Plasmadynamics and Lasers Conference*, AIAA Paper 2008-4214, June 2008.
- [17] Wyckham, C. M., and Smits, A. J., “Aero-Optic Distortion in Transonic and Hypersonic Turbulent Boundary Layers,” *AIAA Journal*, Vol. 47, No. 9, 2009, pp. 2158–2168. doi:10.2514/1.41453
- [18] Wang, K., and Wang, M., “Aero-Optics of Subsonic Turbulent Boundary Layers,” *Journal of Fluid Mechanics*, Vol. 696, April 2012, pp. 122–151. doi:10.1017/jfm.2012.11
- [19] Gordeyev, S., Jumper, E. J., and Hayden, T., “Aero-Optics of Supersonic Boundary Layers,” *AIAA Journal*, Vol. 50, No. 3, 2012, pp. 682–690. doi:10.2514/1.J051266
- [20] DeLuca, N., Gordeyev, S., and Jumper, E. J., “In-flight Aero-Optics of Turrets,” *Journal of Optical Engineering*, Vol. 52, No. 7, 2013, p. 071405. doi:10.1117/1.OE.52.7.071405
- [21] De Lucca, N., Gordeyev, S., and Jumper, E., “Comparison of Aero-Optical Measurements from the Flight Test of Full and Hemispherical Turrets on the Airborne Aero-Optics Laboratory,” *43rd AIAA Plasmadynamics and Lasers Conference*, AIAA Paper 2012-2985, June 2012.
- [22] Wallace, R. D., Shea, P. R., Glauser, M. N., Vaithianathan, T., and Carlson, H. A., “Feedback Flow Control for a Pitching Turret (Part 2),” *48th AIAA Aerospace Sciences Meeting*, AIAA Paper 2010-361, Jan. 2010.
- [23] Cress, J. A., “Optical Distortions Caused by Coherent Structures in a Subsonic Compressible, Turbulent Boundary Layer,” Ph.D Thesis, Univ. of Notre Dame, Notre Dame, IN, 2010.
- [24] Gordeyev, S., Cress, J. A., Jumper, E., and Cain, A. B., “Aero-Optical Environment Around a Cylindrical Turret with a Flat Window,” *AIAA Journal*, Vol. 49, No. 2, 2011, pp. 308–315. doi:10.2514/1.J050476
- [25] De Lucca, N., Gordeyev, S., and Jumper, E., “The Study of Aero-Optical and Mechanical Jitter for Flat Window Turrets,” *50th AIAA Aerospace Sciences Meeting*, AIAA Paper 2012-0623, Jan. 2012.
- [26] Morgan, P., and Visbal, M., “Numerical Simulation Investigating Control of Flow over a Flat Window Turret,” *49th AIAA Aerospace Sciences Meeting*, AIAA Paper 2011-468, Jan. 2011.
- [27] Morgan, P., and Visbal, M., “Simulation of Aero-Optics for Flow over a Flat-Window Hemispherical Turret,” *41st AIAA Fluid Dynamics Conference and Exhibit*, AIAA Paper 2011-3264, June 2011.
- [28] Gordeyev, S., Hayden, T., and Jumper, E., “Aero-Optical and Flow Measurements over a Flat-Windowed Turret,” *AIAA Journal*, Vol. 45, No. 2, 2007, pp. 347–357. doi:10.2514/1.24468
- [29] Gordeyev, S., Cress, J., and Jumper, E., “Far-Field Laser Intensity Drop-Outs Caused by Turbulent Boundary Layers,” *Journal of Directed Energy* (to be published).
- [30] Abado, S., Gordeyev, S., and Jumper, E., “Approach for Two-Dimensional Velocity Mapping,” *Journal of Optical Engineering*, Vol. 52, No. 7, 2013, p. 071402. doi:10.1117/1.OE.52.7.071402
- [31] Smith, A. E., Gordeyev, S., and Jumper, E., “Recent Measurements of Aero-Optical Effects Caused by Subsonic Boundary Layers,” *Journal of Optical Engineering*, Vol. 52, No. 7, p. 071404, 2013. doi:10.1117/1.OE.52.7.071404

L. Cattafesta
Associate Editor